International Journal of Biological Macromolecules 222 (2022) 2467–2478

Contents lists available at ScienceDirect

International Journal of Biological Macromolecules

journal homepage: www.elsevier.com/locate/ijbiomac

Novel chimeric proteins mimicking SARS-CoV-2 spike epitopes with broad inhibitory activity

Mario Cano-Muñoz [a,d], Daniel Polo-Megías [a], Ana Cámara-Artigas [b], José A. Gavira [c], María J. López-Rodríguez [a], Géraldine Laumond [d], Sylvie Schmidt [d], Julien Demiselle [e], Seiamak Bahram [d], Christiane Moog [d,f,*], Francisco Conejero-Lara [a,*]

[a] Departamento de Química Física, Instituto de Biotecnología y Unidad de Excelencia de Química Aplicada a Biomedicina y Medioambiente (UEQ), Facultad de Ciencias, Universidad de Granada, 18071 Granada, Spain
[b] Department of Chemistry and Physics, Agrifood Campus of International Excellence (ceiA3) and CIAMBITAL, University of Almeria, Carretera de Sacramento s/n, 04120 Almeria, Spain
[c] Laboratory of Crystallographic Studies, IACT, CSIC-UGR, Avenida de las Palmeras 4, 18100 Armilla, Granada, Spain
[d] Laboratoire d'ImmunoRhumatologie Moléculaire, Institut National de la Santé et de la Recherche Médicale (INSERM) UMR_S 1109, Institut thématique interdisciplinaire (ITI) de Médecine de Précision de Strasbourg, Transplantex NG, Faculté de Médecine, Fédération Hospitalo-Universitaire OMICARE, Fédération de Médecine Translationnelle de Strasbourg (FMTS), Université de Strasbourg, Strasbourg, France
[e] UMR_S1260, NanoRegMed, University of Strasbourg, Strasbourg, France
[f] Vaccine Research Institute (VRI), Créteil, France

ARTICLE INFO

Keywords:
COVID-19
Fusion inhibitor
Vaccine

ABSTRACT

SARS-CoV-2 spike (S) protein mediates virus attachment to the cells and fusion between viral and cell membranes. Membrane fusion is driven by mutual interaction between the highly conserved heptad-repeat regions 1 and 2 (HR1 and HR2) of the S2 subunit of the spike. For this reason, these S2 regions are interesting therapeutic targets for COVID-19. Although HR1 and HR2 have been described as transiently exposed during the fusion process, no significant antibody responses against these S2 regions have been reported. Here we designed chimeric proteins that imitate highly stable HR1 helical trimers and strongly bind to HR2. The proteins have broad inhibitory activity against WT B.1 and BA.1 viruses. Sera from COVID-19 convalescent donors showed significant levels of reactive antibodies (IgG and IgA) against the HR1 mimetic proteins, whereas these antibody responses were absent in sera from uninfected donors. Moreover, both inhibitory activity and antigenicity of the proteins correlate positively with their structural stability but not with the number of amino acid changes in their HR1 sequences, indicating a conformational and conserved nature of the involved epitopes. Our results reveal previously undetected spike epitopes that may guide the design of new robust COVID-19 vaccines and therapies.

1. Introduction

Since SARS-CoV-2 emerged in late 2019, a huge amount of research developed has increased dramatically our understanding of the molecular basis of the disease and has provided novel strategies to fight it. Vaccines based in immunization with the spike (S) protein, either using mRNA or viral vectors, have been very successful to decrease viral transmission and severity of the disease [1]. However, the immunity of vaccinated people appears to decline after a few months from vaccination and new variants of the virus that may escape the protection of current vaccines appear continuously [2,3]. Moreover, only a limited number of antivirals have been approved to treat the infection, making it essential to continue the development of new treatments and immunization strategies.

As in other coronaviruses, SARS-CoV-2 spike decorates the virus surface and promotes its entry into the host cells. Like other Class-I fusion proteins, the spike protein is a trimer of heterodimers composed of S1 and S2 subunits [4,5] (Fig. 1). The S1 subunit consists of the N-terminal domain (NTD), the receptor-binding domain (RBD) and two C-terminal domains (CTD). Three S1 subunits cover the S2 trimer

Abbreviations: HR1, heptad repeat region 1; HR2, heptad repeat region 2; RBD, receptor binding domain; DSC, differential scanning calorimetry; ITC, isothermal titration calorimetry; CD, circular dichroism; DLS, dynamic light scattering; SLS, static light scattering.

* Corresponding authors.
E-mail addresses: c.moog@unistra.fr (C. Moog), conejero@ugr.es (F. Conejero-Lara).

https://doi.org/10.1016/j.ijbiomac.2022.10.031
Received 28 July 2022; Received in revised form 29 September 2022; Accepted 5 October 2022
Available online 8 October 2022

and lock it in its prefusion conformation. S2 contains a fusion peptide (FP) and two heptad-repeat regions (HR1 and HR2) that are essential to promote membrane fusion. The S2 prefusion structure is organized around a coiled-coil trimer formed by its central helix (CH) and the connector domain (CD), located between the HR1 and HR2 regions. The protein is embedded in the viral membrane by a transmembrane (TM) segment that is followed by an internal short C-terminal tail (CT).

Cell infection by SARS-CoV-2 starts with S1 binding to the angiotensin-converting enzyme 2 receptor (ACE2) using the receptor-binding domain (RBD) (Fig. 1A). Then, proteolysis of the S2 subunit at the S2′ site mediated by host proteases (TMPRSS2 in plasma membrane or Cathepsins in the endosomes [6]) triggers a conformational transition in which HR1 becomes extended to continue the CH trimeric coiled-coil and produces the insertion of FP into the cell membrane [7]. Then, S1 is shed and S2 folds on itself forming six-helix bundle (6-HB) structure (Fig. 1B–C), in which three HR2 pack externally against the hydrophobic grooves of a central trimeric HR1 helical bundle [5,8]. This process brings into close proximity the viral and cell membranes promoting their fusion and subsequent insertion of viral content inside the cell (Fig. 1A).

Because of their importance in viral fusion, HR1 and HR2 are potential targets for coronavirus treatment [8,9]. Moreover, these regions have particularly high sequence conservation in SARS-CoV-2 [10], as well as between different coronaviruses [9,11]. Current high-resolution structures of the pre-fusion spike do not resolve the S2 stalk region connecting the S head with the transmembrane region [4], although it has been characterized as highly flexible [12], with two coiled-coil regions separated by flexible hinges [13]. Interestingly, the SARS-CoV-2 spike is highly glycosylated [14,15] and HR2 contains two N-glycosilation sites at residues Asn1173 and Asn1194, which may protect this highly preserved region from antibody access, although its flexibility could make it vulnerable to other types of molecules and small compounds.

S2-mediated fusion of SARS-CoV-2, as well as other coronaviruses, is inhibited by peptides derived from HR2 [8,9,16,17], similarly to that observed for gp41 mediated HIV-1 fusion [18,19]. HR1-based peptides are much less potent inhibitors [16,17] but stabilized mimics of a

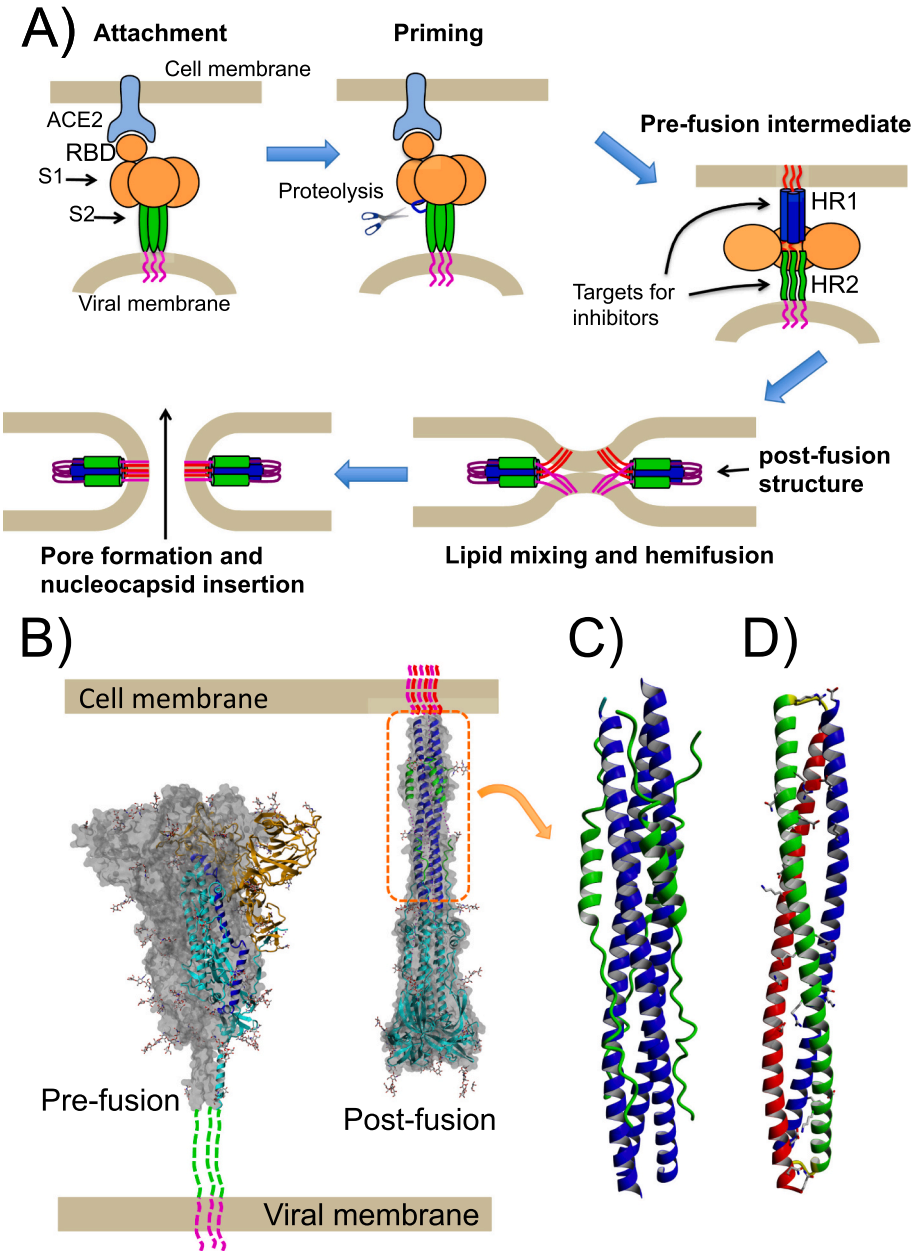

Fig. 1. Fusion mechanism of SARS-CoV-2 and Spike structure. A) Schematic drawing of the fusion mechanism of the SARS-CoV-2 with the host cell membrane. B) Cryo-EM pre-fusion and post-fusion structures of the Spike ectodomain (PDB id. 6XR8 and 6XRA [5]). Two S1/S2 heterodimers in the pre-fusion spike are represented with grey molecular surface, whereas one of the heterodimers has been represented with ribbons. The S1 subunit is colored in orange. The HR1 region is colored in blue and the rest of the S2 subunit is colored in cyan. The HR2 region in the spike stem is not resolved in the structure and is indicated with the dashed green line. The transmembrane region and the C-terminal tail are colored in magenta. The glycans decorating the spike surface are represented with sticks. The dashed box in the post-fusion structure indicates the 6-helix bundle formed by the HR1 and HR2 regions. C) Post-fusion core structure (PDB id. 6LXT [8]) showing the six-helix bundle complex between HR1 (blue) and HR2 (green). D) Ribbon model of the single-chain chimeric CoVS-HR1 proteins mimicking the S2 HR1 region. The three consecutive helices are colored in blue, green and red, respectively. The loops connecting the helices are colored in yellow. Side chains of amino acids engineered to create stabilizing interactions are highlighted with sticks (see main text for details).

trimeric helical bundle based on the HIV-1 gp41 HR1 that target HR2 have shown potent inhibitory activity of HIV-1 fusion [20–22] and also inhibit human coronaviruses [23]. Moreover, a 5-helix construct based on the S2 6-HB structure but lacking one HR2 region has been reported very recently to inhibit several SARS-CoV-2 variants [24]. Also, trimers of S2 HR1 polypeptides stabilized by conjugation to a foldon sequence (HR1MFd) show broad coronavirus inhibitory activity [25]. All this evidence indicates that both HR1 and HR2 are exposed during coronavirus fusion and susceptible to inhibition, as it has been reported for HIV-1. Vaccination with stabilized gp41 HR1 trimers can elicit neutralizing antibodies against HIV-1 [26] and HIV-1 infected patients elicit neutralizing antibodies that target exposed HR1 epitopes [27,28]. Moreover, human mAbs directed against HR1 and HR2 regions of SARS-CoV show broad neutralizing activity [29]. Given the similarities between the class-I proteins mediating viral fusion mechanisms, it is conceivable that similar antibody responses may be elicited during SARS-CoV-2 infection. However, this type of antibody responses has so far passed unnoticed.

Antibody responses produced by SARS-CoV-2 infection are mostly induced against the nucleocapsid protein and the spike protein and, within this, against the S1 subunit [30,31]. Neutralizing Ab responses in COVID-19 convalescent patients are mainly directed to the RBD but mutations in emerging SARS-CoV-2 variants drastically reduce their neutralization potential [3,32,33]. Neutralizing responses targeting S2 are scarcer than those against S1 but they are more interesting [34] because S2 is more conserved than S1. Moreover, S2-targetting neutralizing antibody responses that cross-react with other related coronaviruses have been reported, even in uninfected individuals [35]. This type of memory B cell immunity may confer durable broad coronavirus protection [36].

Epitope mapping has so far detected only a few immunogenic linear epitopes in S2 [37] mostly located at sequence region 765–835, comprising the FP and the S2 cleavage site, and residues 1140–1160 at the S2 stem region immediately upstream of HR2. Both epitopes have been described as neutralizing [38,39]. There is however a lack of highly immunogenic epitopes within HR1 and HR2 described in the literature. A possible reason is that HR1 and HR2 are highly protected from the immune system due to their importance in the conformational changes driving membrane fusion. It is also possible that conformational variability of these regions could make their sensitive epitopes to be only transiently exposed and poorly immunogenic. Nonetheless, immune responses to conformational epitopes may have gone unnoticed in epitope mapping studies using linear peptides.

We previously designed HR1 mimetic proteins targeting HIV gp41 [22,40–44]. These chimeric proteins consist in single polypeptide chains that stably and spontaneously fold as trimeric helical bundles with helix-loop-helix-loop-helix topology. These proteins imitate accurately an exposed HR1 groove and tightly bind to gp41 HR2 peptides with identical HR1-HR2 interactions to the post-fusion gp41 structure [42,43]. Moreover, the proteins have a potent and broad inhibitory activity against a variety of HIV-1 strains [22,40,42,44,45]. Because of the structural similarities between the post-fusion structures of gp41 and S2, we hypothesized that similar single-chain chimeric proteins could be designed to mimic an exposed SARS-CoV-2 HR1 and that these proteins could also have antiviral activity.

2. Materials and methods

2.1. Molecular modeling

Modeling was carried out using SwissPDBviewer [46] and YASARA structure [47]. As template, we used the published X-ray crystal structure of the six-helical bundle formed by HR1 and HR2 in the S2 post-fusion structure (PDB id. 6LXT [8]; Fig. 1C). To model an antiparallel trimer of helices, the HR2 chains were deleted from the model and one of the HR1 helices (Spike residues 914–988) was turned around and aligned with the original one. Due to the antiparallel orientation of the reversed helix, the side chain CA-CB bonds have different spatial orientation compared the native parallel one. This could produce improper side chain packing with the other helices in the coiled-coil structure. To compensate this, the helix alignment was made superimposing the CB atoms of the core residue side chains. To preserve the correct core coiled-coil packing, the amino acid sequence of the upturned helix was also reversed. Then, side chain clashes were removed by energy minimization. Four-residue loops were manually built to connect each pair of helix termini to create a helix-loop-helix-loop-helix topology. The chimeric proteins were generically named CoVS-HR1 (Figs. 1D and 2). The amino acid composition of the loops was selected using the built model with RossetaDesign web server (http://rosettadesign.med.unc.edu [48]).

To enhance the stability of the antiparallel trimeric bundle and reduce exposed hydrophobicity, several surface-exposed residues at *e* and *g* positions of the coiled-coil heptad repeats were replaced by charged or polar amino acids to engineer proper salt bridges and hydrogen bonds between the antiparallel helix and the other two helices. Additional mutations at solvent exposed positions were made to increase net positive charge. No mutations were carried out to modify the hydrophobic groove between the two parallel HR1 helices to preserve the HR2 binding potential. The engineered residue positions were rationally selected by visual analysis of the model. Two variants code-named L3A and L3B were engineered using different sets of amino acid substitutions (Fig. 2). The choice of amino acid substitutions was made rationally for L3A, whereas for L3B amino acid substitutions were selected with the aid of RossetaDesign. A third variant, code-named L3C, was engineered from the L3B variant by substitution of glycine residues (Fig. 2, Table S1) in the middle of α-helical regions for polar side chains, which were also selected with RossetaDesign. Finally, all the models were subjected to energy minimization. The amino acid sequences are collected in Table S1.

2.2. Protein production and HR2 peptides

The DNA encoding the protein sequences were synthesized and cloned into pET303 expression vectors by Thermo Fisher Scientific (Waltham, MA, USA), including a N-terminal methionine and a C-terminal polyhistidine tag with sequence GGGGSHHHHHH. The proteins were overexpressed in *E. coli* bacteria (BL21(DE3)) and purified following a two-step chromatography protocol, adapted from the method described previously [22]. Specific details of the protein production protocol are described in the Supplementary Material. Protein purity (>95 %) was assessed by SDS-PAGE and the identity of each protein was confirmed by mass spectrometry.

Synthetic peptide V39E derived from the S2 HR2 sequence was acquired from Genecust (Luxembourg), with a purity >95 %. The peptide (residues 1164–1202) was C-terminally tagged with a SGGY sequence to confer UV absorption at 280 nm, as well as *N*-acetylated and C-amidated. Protein and peptide concentrations were measured by UV absorption measurements at 280 nm with extinction coefficients calculated according to their respective amino acid sequences with the Expasy ProtParam server (https://web.expasy.org/protparam/) [49].

2.3. Circular dichroism (CD)

CD measurements were performed with a Jasco J-715 spectropolarimeter (Tokyo, Japan) equipped with a temperature-controlled cell holder. Typical protein concentration was 15 μM. Measurements of the far-UV CD spectra (260–200 nm) were made with a 1 mm path length quartz cuvette. Spectra were recorded at a scan rate of 100 nm/min, 1 nm step resolution, 1 s response and 1 nm bandwidth. The resulting spectrum was usually the average of 5 scans. Each spectrum was corrected by baseline subtraction using the blank spectrum obtained with the buffer and finally the CD signal was normalized to molar

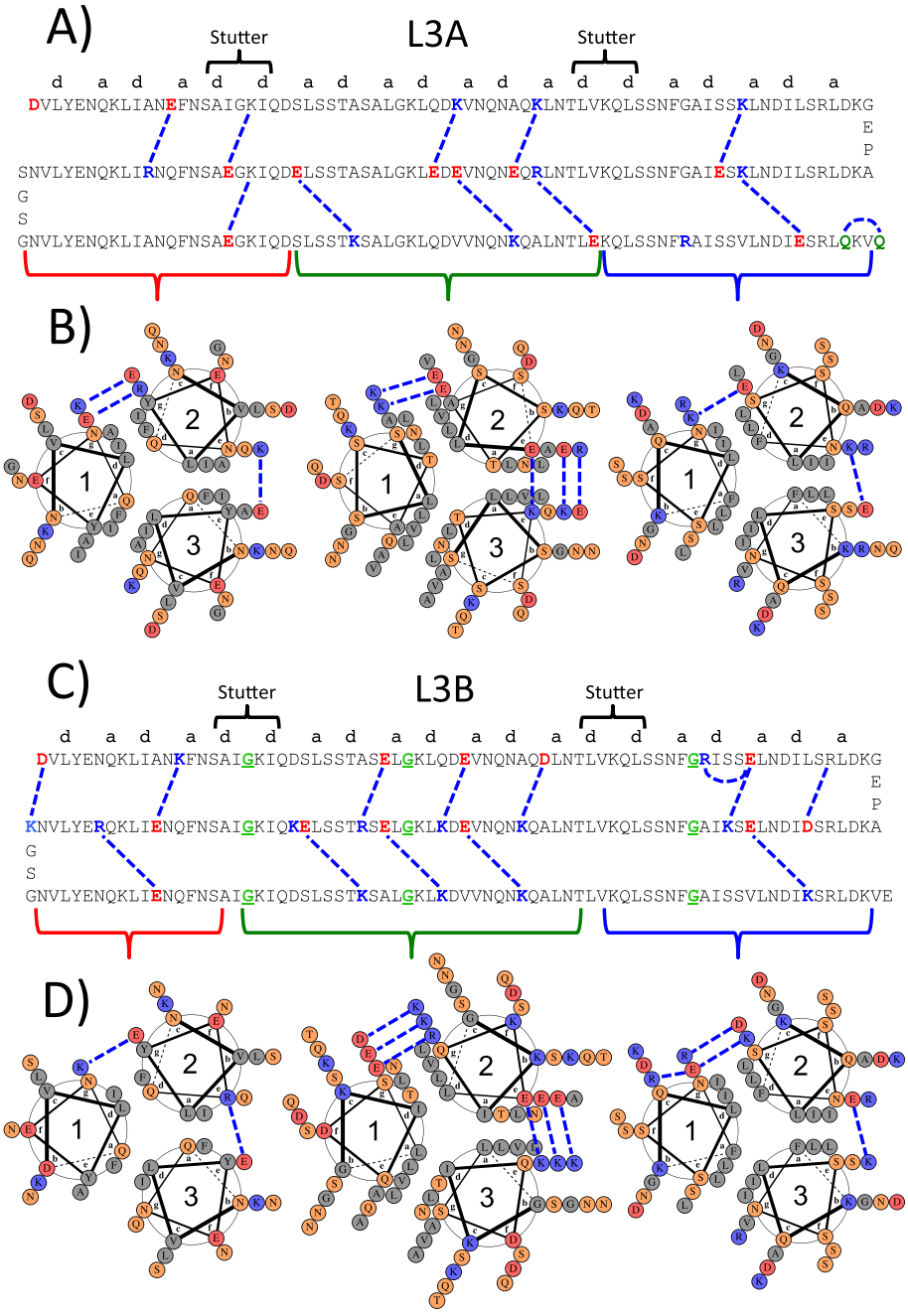

Fig. 2. Sequence and topology of CoVS-HR1 proteins. A) and C) Sequence and topology of L3A variant (A) L3B (C) indicating the engineered amino acid substitutions (highlighted with colors) and the stabilizing interactions (with blue dashed lines). The 'a' and 'd' characters on top of the first sequence stretch indicate the corresponding positions in a heptad repeat. Two stutters in the canonical repeats are indicated. B) and D) Helix-wheel diagrams corresponding to three different sections of the coiled-coils in L3A (B) and L3B (D) (indicated with brackets). The glycine amino acids substituted for polar amino acids in the L3C variant are underlined and highlighted in green over the L3B sequence. The diagrams have been drawn with Drawcoil (https://grigoryanlab.org/drawcoil/). The blue dashed lines indicate the engineered stabilizing interactions in each molecule.

ellipticity ([θ], in deg·cm^2·dmol^{-1}). Thermal unfolding was monitored by measuring the CD signal at 222 nm as a function of temperature using a scan rate of 2 °C·min^{-1}.

2.4. Molecular size characterization

The apparent hydrodynamic radii of the proteins were measured using dynamic light scattering (DLS) in a DynaPro MS-X DLS instrument (Wyatt, Santa Barbara, CA). Dynamics v6 software (Wyatt Technology Corporation, Santa Barbara, CA) was used in data collection and processing to obtain the hydrodynamic radii distributions. The expected hydrodynamic radius for the monomers was estimated about 3.3 nm with Hydropro software using the computer models of the proteins [50]. Sets of DLS data were measured at 25 °C with an average number of 50 acquisitions and an acquisition time of 10 s.

Static scattering intensities were measured in a DynaPro MS-X DLS instrument (Wyatt, Santa Barbara, CA) or a Malvern μV instrument (Malvern Panalytical, Malvern, UK) at 25 °C, in 50 mM sodium phosphate buffer pH 7.4, at different concentrations of protein in a range of 0.2–4.5 mg·mL^{-1}. The intensities were analyzed using the Debye plot as represented by Eq. (1),

$$K \cdot c / R_{90} = 1/M_w + 2A_2 c \quad (1)$$

valid for particles significantly smaller than the wavelength of the incident radiation, where K is an optical constant of the instrument, c is the particle mass concentration, R_{90} is the Rayleigh ratio of scattered to incident light intensity, M_w is the weight-averaged molar mass, A_2 is the 2nd virial coefficient that is representative of inter-particle interaction strength. M_w can be determined from the inverse of the intercept.

2.5. Differential scanning calorimetry

DSC experiments were carried out in a MicroCal PEAQ-DSC microcalorimeter equipped with autosampler (Malvern Panalytical, Malvern, UK). Scans were run from 5 to 130 °C at a scan rate of 90 °C·h^{-1}. Protein concentration was typically 30 μM. Instrumental baselines were recorded before each experiment with both cells filled with buffer and subtracted from the experimental thermograms of the protein samples. Consecutive reheating runs were carried out to determine the reversibility of the thermal denaturation. The excess heat capacity (ΔC_p) relative to the buffer was calculated from the experimental DSC thermograms using Origin software (OriginLab, Northampton, MA).

2.6. Isothermal titration calorimetry

ITC measurements were carried out in a Microcal VP-ITC calorimeter (Malvern Panalytical, Malvern, UK). The proteins were titrated with 25 injections of 5 μL peptide solution at 480 s intervals. Protein concentration in the cell was around 10 μM, unless stated otherwise, while the peptide concentration in the syringe was typically 200–400 μM. The experiments were carried out in 50 mM phosphate buffer (pH 7.4) at 25 °C. The experimental thermograms were baseline corrected and the peaks were integrated to determine the heats produced by each ligand injection. Residual heats due to unspecific binding or ligand dilution were estimated from the final peaks of the titrations. Each heat was normalized per mole of injected ligand. The resulting binding isotherms were fitted using a binding model of n independent and equivalent sites, allowing the determination of the binding constant, K_b, the binding enthalpy, ΔH_b, and the binding stoichiometry, n. The standard Gibbs energy and entropy of binding were calculated according to Eq. (2).

$$\Delta G_b = -RT \cdot lnK_b = \Delta H_b - T \cdot \Delta S_b \quad (2)$$

2.7. Protein crystallization

Freshly purified CoVS-HR1 protein was dialyzed against 10 mM Tris pH 7.5 buffer and concentrated to ≈9 mg·mL^{-1}. The V39E peptide was weighted and dissolved in deionized water. The pH was adjusted to pH 7.5, the solution was centrifuged at 14,000 rpm in a microfuge for 30 min at 4 °C and its concentration was measured by UV absorption at 280 nm. Then, the necessary volume to achieve the desired peptide quantity was transferred to a clean microtube and lyophilized. Complex solutions (1:2 protein:peptide ratio) were prepared by dissolving the lyophilized peptide prepared previously with the appropriate volume of protein solution. After 15–20 min equilibration, the solution was again centrifuged at 14,000 rpm for 30 min.

Screening for initial crystallization conditions was performed by the sitting-drop vapor-diffusion method using commercially available crystal screening kits Structure 1 and 2 Eco Screen from Molecular Dimensions (Suffolk, UK). Droplets consisting of 2 μL complex solution and 2 μL reservoir solution were equilibrated at 298 K against 200 μL reservoir solution in 48-well MRC Maxi Optimization plates (Cambridge, UK). Several favorable conditions were initially identified and were optimized to obtain crystals. The best diffracting crystals were obtained in 0.1 M sodium HEPES pH 7.5, 20 % (w/v) PEG4000, 10 % (v/v) isopropanol.

2.8. Diffraction data collection, structure solution and refinement

For data collection, crystals were flash-cooled in liquid nitrogen. Data sets were collected at 100 K at the beamline XALOC at the ALBA synchrotron (Barcelona, Spain), using a wavelength of 0.97926 Å [51]. Diffraction data were indexed and integrated with the AutoPROC toolbox [52]. Data scaling was performed using the program Aimless [53] from the CCP4 suite [54]. Data collection statistics are collected in Table S2. Solution and refinement of the structures were performed using the PHENIX suite [55]. Molecular-replacement phasing using PHASER [56] was performed with the coordinates of the crystallographic structure of post fusion core of 2019-nCoV S2 subunit (PDB entry 6LXT [8]). Manual model building was performed using COOT [57,58]. Refinement was performed using phenix.refine in PHENIX [59]. The quality of the structures was checked using MOLPROBITY [60] and PDB_REDO [61]. Structural refinement statistics are collected in Table S2. All residues are in the allowed region of the Ramachandran plot. The complex coordinates were deposited at the Protein Data Bank under the accession code 7ZR2.

2.9. S protein binding assays

CoVS-HR1 proteins ability to bind soluble trimeric Spike (S) proteins was determined by ELISA. Briefly, 96-well ELISA plates (Maxisorp, Nunc) were coated at 4 °C overnight with recombinant trimeric SARS-CoV-2 Spike protein (ProSci Inc., Poway, CA, Catalog Number 10-075, Spike sequence Gln14 - Gln1208, Protein Accession Number: QHD43416.1) in 0.1 M bicarbonate buffer (pH 9.6). This recombinant protein corresponds to the uncleaved Spike ectodomain truncated after HR2, so devoid of the TM and CT regions. After saturation with 2 % BSA, 0.05 % Tween in PBS for 1 h at 25 °C, 0.3–8.0 nM of CoVS-HR1 molecules (100 μL diluted in 1 % BSA 0.05 % Tween solution) were added and incubated for 2 h at room temperature. The plate was then washed five times and CoVS-HR1 binding was detected with 100 μL anti-6× Histag antibody conjugated to horseradish peroxidase (HRP) (Abcam, Cambridge, UK) at 1/10,000 dilution incubated for 1 h at room temperature. Antibody binding was then revealed with tetramethylbenzidine (TMB) substrate buffer, the reaction was stopped with 1 M H_2SO_4 and optical density was read at 450 nm with a Molecular Device Plate Reader equipped with SoftMax Pro 6 program. Background binding was measured in plates without Spike protein and subtracted from the data. The percentage of binding was calculated using the readings with wells coated with His-tagged Spike incubated with PBS buffer instead of CoVS-HR1 molecules as control for 100 % binding. Half maximal binding effective concentration (EC_{50}) was calculated by fitting the data using a Hill's sigmoidal function.

2.10. Virus inhibition assays

One-day prior infection, Vero 76 cells were plated on a 96 well plate at 12,500 cells/well. 50 μL of serial 4-fold dilutions of CoVS-HR1 proteins (2-fold concentrated) and 50 μL WT SARS-CoV-2 viruses (B1 UK D614G or BA.1 Omicron genotypes) at Multiplicities Of Infection (MOI) of 80 were added to the cells. After 2 days of culture, cells were fixed with methanol for 20 min, washed with PBS and stained with anti-Nucleocapside Antibody (Genetex, Irvine, CA, GTX135357) at 1/200 dilution in permwash (B&D) for 45 min at room temperature. Ab was revealed by incubation with a donkey anti-Rabbit monoclonal Ab (Alexa 647; A31573, Invitrogen, Waltham, MA) diluted at 1/200 in PBS 5 % FCS for 45 min at room temperature. In parallel, total alive cells were detected by Sytox green (S7020, Invitrogen, Waltham, MA) staining allowing the quantification of any cytotoxicity produced by the proteins. Total cells (Sytox green positive) and infected cells (nucleocapside positive) were counted using SpectraMax MiniMax Imaging Cytometer (Molecular Devices LLC, San Jose, CA). The percentage of infected cells in each well was calculated by comparing the number of infected cells with the total number of living cells. Thereafter, the percentage of inhibition was calculated from the reduction in the percentage of infected cells in wells treated with inhibitor relative to the percentage of infected cells in control wells not treated with inhibitor using the formula:

$$\%Inhibition = 100 \cdot \frac{100 - \%\text{infected}\,cells\,(treated)}{\%\text{infected}\,cells\,(control\ untreated)} \quad (3)$$

The 50 % inhibitory concentration (IC_{50}) was defined as the protein concentration leading to a 50 % reduction in the percentage of infected

cells. IC_{50} was estimated by fitting the data using a Hill's sigmoidal function.

2.11. Detection of antibody responses in patients' sera

CoVS-HR1 antigenicity against sera of infected patients was determined by ELISA. Sera samples were collected 3 months after recovery from COVID-19 infection. All patients and healthy donors gave their written informed consent (COVID-HUS ethics committee approved, reference CE: 2020-34). 96-Well ELISA plates (Maxisorp, Nunc) were coated at 4 °C overnight with 0.5 μM CoVS-HR1 proteins or recombinant RBD (Interchim, Montluçon, France) in 0.1 M bicarbonate buffer (pH 9.6). After blocking with 5 % non-fat powdered milk in PBS for 1 h at 25 °C, 1/1000 diluted sera of patients collected after 3 months of

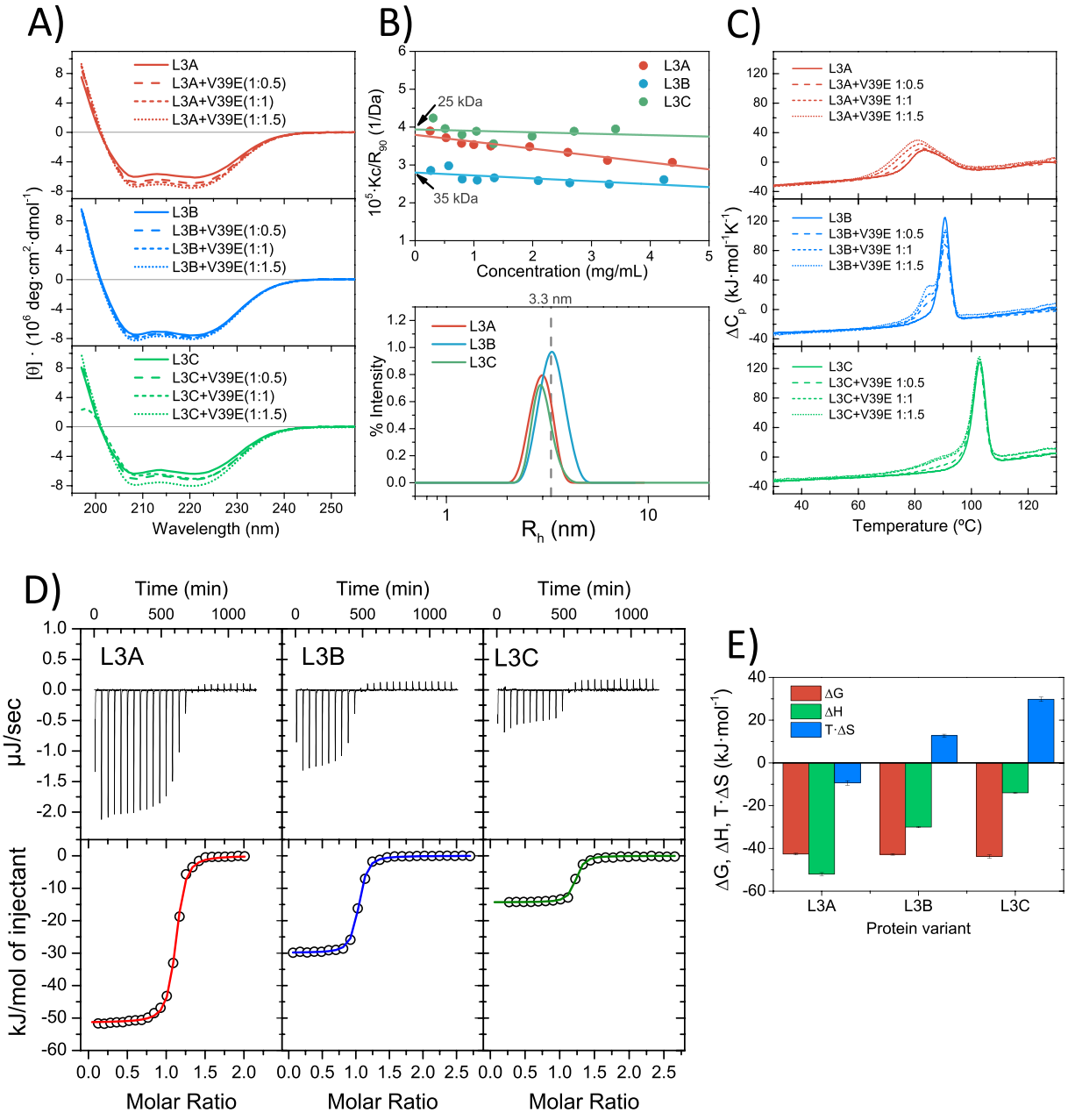

Fig. 3. Biophysical characterization of CoVS-HR1 mimetic proteins. A) Far-UV circular dichroism (CD) spectra showing highly α-helical structures for the three protein variants. The spectra were recorded at 25 °C, 15 μM protein concentration and pH 7.4 and were normalized per mole of protein for proper comparison. Addition of HR2-derived V39E peptide increases slightly the α-helical structure content due to its binding to the proteins in a partially helical conformation. B) Particle size analysis by light scattering. Upper panel shows the Debye plot made from scattering intensity measurements as a function of the protein concentration. The intercepts indicate the mean-weighted molar masses. The expected molar masses of the protein monomers are 26.4 kDa (L3A), 26.5 kDa (L3B) and 27.1 kDa (L3C). Lower panel shows the hydrodynamic radius distributions measured by dynamic light scattering. The expected hydrodynamic radius for the monomers was estimated about 3.3 nm. C) Thermal stability analysis by differential scanning calorimetry (DSC). The denaturation peaks indicate high thermal stability for the three protein variants. The thermograms measured in presence of V39E peptide show endothermic pre-transitions due to the dissociation of the peptide from the complex. D) Isothermal titration calorimetry (ITC) analysis of the binding of the HR2-derived V39E peptide to the different CoVS-HR1 proteins. The upper panels show the experimental thermograms with negative heats of binding. The lower panels show the normalized binding isotherms fitted using a model of independent binding sites. The binding stoichiometry is 1:1. E) Thermodynamic magnitudes of binding of the HR2 peptide to each protein variant calculated from the ITC data (Table 1). Error bars correspond to 95 % confidence intervals of the parameters estimated from the fits in panel D.

infection (100 μL diluted in 1 % BSA 0.05 % Tween solution) were added and incubated for 30 min at room temperature. The plate was then washed five times and CoVS-HR1 binding antibodies (IgG or IgA) were detected with 100 μL goat anti-human (IgG or IgA) antibody conjugated to horseradish peroxidase (HRP) (Abcam, Cambridge, UK) at 1/5000 dilution incubated for 1 h at room temperature. Antibody binding was then revealed with tetramethylbenzidine (TMB) substrate buffer, the reaction was stopped with 1 M H_2SO_4 and optical density was read at 450 nm with a Molecular Device Plate Reader equipped with SoftMax Pro 6 program. Background binding was measured in plates without CoVS-HR1 proteins and subtracted from the data. As positive control His-tagged RBD was used to detect the anti-RBD antibodies present in the patients sera. Control sera from healthy patients were also assayed. Data was analyzed using Origin software (OriginLab, Northampton, MA).

3. Results

3.1. Design and production of SARS-CoV-2 HR1 mimetic proteins

We designed several single-chain proteins imitating the coiled-coil structure of the SARS-CoV-2 HR1 trimer using a similar strategy as previously employed with HIV-1 gp41 [22]. The chimeric proteins, subsequently named CoVS-HR1, were designed as antiparallel helical bundles with a helix-loop-helix-loop-helix topology (Fig. 1D), in which the second helix was reversed in both sequence and spatial orientation. The helices were tethered with manually built four-residue loops. Then, three different variants (code-named L3A, L3B and L3C) were created carrying out different sets of amino acid substitutions in order to stabilize their trimeric coiled-coil structure (Fig. 2). L3A and L3B carried different amino acid substitutions and L3C was derived from L3B by substitution of glycine residues in the middle of α-helices for polar side chains with higher helical propensity (Fig. 2C; see also Materials and methods and Table S1 for details).

The CoVS-HR1 proteins were produced in recombinant form by overexpression in *E. coli* with high yields and could be easily purified by two-step standard chromatographic methods. All the proteins were highly soluble in different standard buffers ($\geq$10 mg·mL^{-1} in 50 mM sodium phosphate pH 7.4) and acquired spontaneously the predicted α-helical structure according to their circular dichroism (CD) spectra (Fig. 3A). The percentage of α-helix, estimated from the mean-residue ellipticity at 222 nm [62], varied with pH (Fig. S1A–C). Highest α-helix content occurred at intermediate pH and was consistent with 90 % helical residues as estimated from the models. Thermal scans monitored by CD showed high temperature unfolding transitions with secondary structure loss (Fig. S1D–F), except for L3C at pH 6 and pH 7.4, which shows melting temperatures above 100 °C.

The proteins showed an apparent hydrodynamic radius (R_h) with small variations depending on the pH and in close agreement with a monomeric state (R_h is estimated in 3.3 nm using the protein models) under most conditions according to DLS measurements (Figs. 3B and S2). Debye plots using SLS measurements at pH 7.4 yielded M_w values corresponding to monomers for L3A and L3C, whereas L3B showed an apparent M_w between the monomer and the dimer (Fig. 3B), suggesting a slight tendency to self-association. L3B showed more asymmetric hydrodynamic radius distributions with minor contributions of larger particles (Fig. S2E). L3A also showed slightly higher hydrodynamic radius at high concentrations (Fig. S2D). However, these deviations from the monomeric state only occur at relatively high protein concentrations of low biological relevance.

The three proteins were very stable against thermal denaturation monitored by differential scanning calorimetry (DSC), showing melting temperatures above 80 °C at pH 7.4 (Fig. 3C). Maximum stability was observed at pH 6 and 7.4 and decreased at acid and basic pH (Fig. S3). L3B and L3C showed larger and sharper denaturation peaks than L3A, indicating more stable and cooperative structures in the two former variants. Among them, L3C was more thermostable than L3B by about 13 °C, as a result of higher α-helical propensity of its sequence produced by substitution of glycine residues. The unfolding transitions at pH 7.4 were irreversible as observed in second consecutive DSC scans with the same samples (Fig. S4).

3.2. Binding of CoVS-HR1 proteins to the S2 HR2 region

Binding of the CoVS-HR1 proteins to the HR2-derived peptide V39E (spike sequence 1164–1202) slightly increased the α-helix structure, as observed in the CD spectra (Fig. 3A). In presence of the HR2 peptide, the denaturation peaks of the three proteins in the DSC thermograms were significantly modified, showing the appearance of clear shoulders on the low-temperature side of the unfolding transitions, as a result of endothermic peptide dissociation preceding the unfolding of the proteins (Fig. 3C). Titration of the proteins with the V39E peptide by isothermal titration calorimetry (ITC) showed sigmoidal binding isotherms with 1:1 binding stoichiometry, dissociation constants in the low nM range and considerably negative binding enthalpy (Fig. 3D and Table 1). Interestingly, although the binding affinities to the HR2 peptide varied only slightly for the three protein variants (Table 1), the favorable binding enthalpy decreased in magnitude in the order L3A > L3B > L3C, whereas the binding entropy changed from negative to positive with the same order, indicating a strong enthalpy-entropy compensation (Fig. 3E). This suggests that complex formation involves an entropy cost contribution due to considerable conformational tightening of the HR1 helical bundle, as previously observed for homologous HIV-1 gp41-HR1 mimetic proteins [40,43]. This entropy penalty decreases, however, as a result of a higher intrinsic stability of the HR1 helical bundle in the most stable variant L3C and the binding becomes entropically favored.

To investigate the structural details of the interaction between the CoVS-HR1 proteins and their HR2 target we produced crystals of the L3B and L3C proteins in complex with the V39E peptide. Crystals of good quality for X-ray diffraction could only be obtained for the L3B-V39E complex. Crystals of the free proteins and the L3C-V39E complex did not allow obtaining good quality datasets for structural resolution. Diffraction data were collected to 1.45 Å resolution (Table S2) allowing a very detailed structure characterization (Fig. 4). The structure of the L3B protein is highly similar to the designed model (Figs. 1 and 4A). The conformation of the V39E peptide in the complex and the interactions at the protein-peptide interface were virtually identical to those observed between HR1 and HR2 in the post-fusion S2 structure [8] (Fig. 4B–C). The high resolution of the structure allowed the visualization of fine details of the HR1-HR2 interface (Fig. S5). The interaction is the result of a large number of hydrophobic HR2 residues that insert their side chains along the narrow HR1 crevice, flanked by a considerable number of hydrogen bonds and electrostatic interactions, some of them involving interfacial water molecules. Moreover, the HR1 coiled-coil contains several water-filled internal cavities that establish hydrogen-bond networks with HR1 buried polar residues (Fig. S6).

The three protein variants also bound strongly to recombinant

Table 1
Thermodynamic parameters of binding between CoVS-HR1 proteins and HR2 V39E peptide measured by ITC.

Protein variant	n	K_b (·10^7 M^{-1})	K_d (nM)	ΔH_b (kJ mol^{-1})	$T\cdot\Delta S_b$ (kJ mol^{-1})	ΔG_b (kJ mol^{-1})
L3A	1.09	3.0 ± 0.5[a]	34 ± 5	−52.0 ± 0.7	−9.4 ± 1.1	−42.3 ± 0.4
L3B	1.00	3.2 ± 0.5	32 ± 5	−30.0 ± 0.3	+12.8 ± 0.7	−42.8 ± 0.4
L3C	1.18	4.7 ± 1.4	21 ± 6	−14.0 ± 0.3	+29.8 ± 1.0	−43.8 ± 0.7

[a] Errors in the parameters are estimated as 95 % confidence intervals in the parameters obtained from the fittings using a binding model of n independent and equivalent sites.

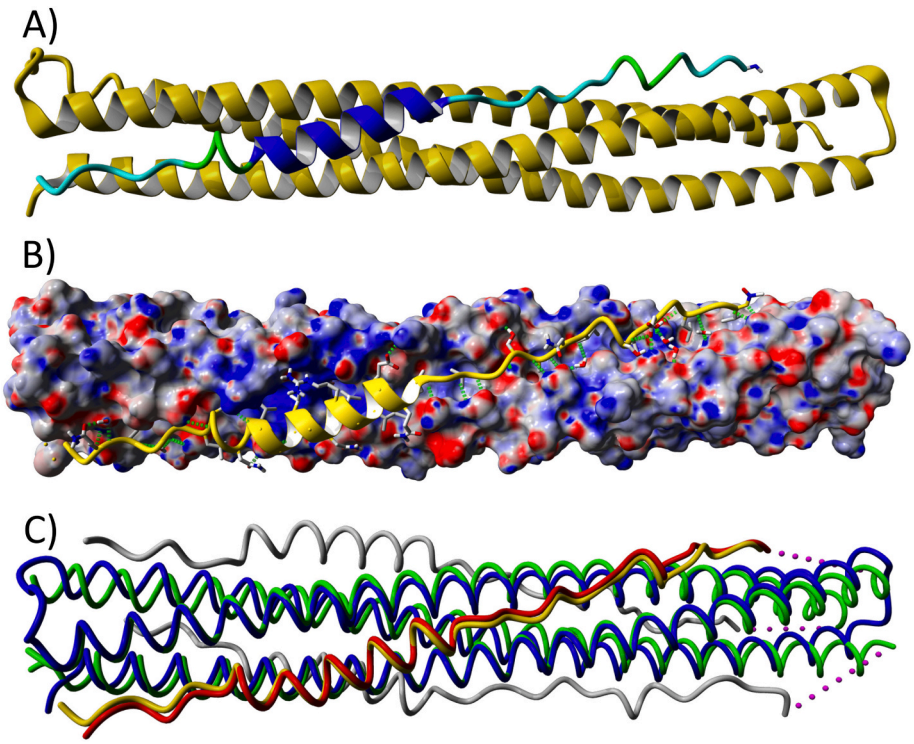

Fig. 4. Crystal structure of the CoVS-HR1-L3B protein in complex with the HR2 V39E peptide. A) Ribbon representation showing the backbone topology and secondary structure of the complex. The L3B protein is colored in yellow and the V39E peptide in color gradation from blue to green according to helical structure. B) Molecular surface of the L3B protein colored according to the electrostatic potential with red indicating negative, white neutral and blue positive. The V39E peptide is represented with a yellow ribbon. The side chains of the peptide and interfacial water molecules that interact with the protein have been highlighted with sticks colored in CPK scheme. The protein-peptide interaction is highly hydrophobic along the binding crevice, flanked by polar and electrostatic interactions at along the edges. Interfacial hydrogen bonds are represented with green dashed lines. C) Structure alignment between the CoVS-HR1-V39E complex (blue and yellow) and the HR1-HR2 post-fusion complex structure (green and red) (PDB id. 6LXT [8]). Alignment was made using the MUSTANG algorithm [72] implemented in YASARA software with 142 matching residues corresponding to the two parallel HR1 helices (helix 1 and 3) of the CoVS-HR1 protein and the HR2 V39E peptide. RMSD between the two structures was 1.0 Å.

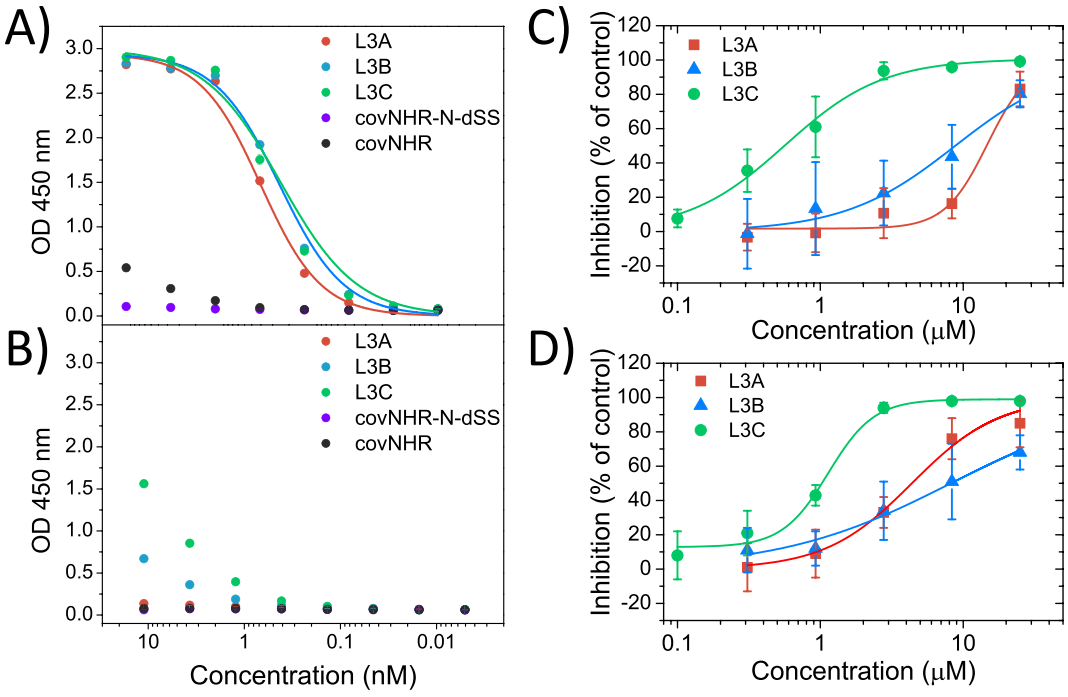

Fig. 5. SARS-CoV-2 inhibition by interaction of CoVS-HR1 proteins with HR2. A) Strong binding of the CoVS-HR1 proteins to recombinant trimeric spike. ELISA plates were coated with trimeric spike and tested with 0.3–8.0 nM CoVS-HR1 proteins or with homologous HIV-1 gp41-HR1 mimetic proteins [40,43]. Binding was detected with anti-6× His-tag antibody conjugated to horseradish peroxidase. Binding of gp41-HR1 mimetic proteins was negligible. B) Similar ELISA experiment was performed in presence of HR2 V39E peptide in a 2:1 peptide:protein ratio. Binding was strongly inhibited for all proteins. C, D) Inhibition of SARS-CoV-2 virus infection by the CoVS-HR1 proteins. Vero 76 cells were infected by primary viruses (B1 D614G genotype, panel C, and Omicron BA.1, panel D) in the presence of CoVS-HR1 proteins at different concentrations. The percentage of inhibition was calculated by reduction in the percentage of infected cells treated with the inhibitory proteins compared to untreated control cells. Data correspond to mean ± standard deviations of 4 independent experiments. Continuous lines correspond to non-linear regression curves using a sigmoidal Hill's function.

trimeric spike in ELISA assays (Fig. 5A). EC_{50} values were 0.4 nM for L3A, 0.25 nM for L3B and 0.25 nM for L3C. At the respective EC_{50} values, their binding to the trimeric spike was competitively inhibited by addition of the V39E peptide (Fig. 5B) indicating that the binding was specific of the HR2 target region. Moreover, other chimeric proteins that mimic HIV-1 gp41 HR1 [42,45] did not show significant binding. Residual binding in presence of competing V39E peptide varied in the order L3C > L3B > L3A, consistently with their relative stabilities.

3.3. Inhibition of SARS-CoV-2 infection

Because the CoVS-HR1 proteins could establish strong interactions with the HR2 region that are structurally similar to those driving membrane fusion, we tested their capacity to inhibit cell infection by SARS-CoV-2. Vero 76 cells were infected with SARS-CoV-2 primary viruses (B1 D614G and BA.1 Omicron genotypes) in presence and absence of CoVS-HR1 proteins (Fig. 5C–D). The three proteins showed inhibitory activity against both viruses without producing toxicity in the cells, as observed by measuring the effect of the proteins on the total number of living cells in the assays (Fig. S7). The average IC_{50} values estimated for L3C from several independent experiments was 0.6 ± 0.1 μM against B1 D614G viruses and 1.1 ± 0.1 μM for BA.1 Omicron. The IC_{50} values of the L3A and L3B proteins were considerably higher and ranged between 4 μM and >10 μM. These results indicated that the proteins recognize the conserved HR2 target sequence in the two strains and thereby block the conformational transition of S2 that promotes membrane fusion and infection. Strikingly, despite a similar binding affinity for the HR2 peptide, L3C showed much higher inhibitory activity for both virus variants than L3A and L3B. This highlights the importance of conformational stability of the HR1 helical bundle in these designs.

3.4. CoVS-HR1 proteins detect antibody responses against SARS-CoV-2 infection

Since the CoVS-HR1 proteins faithfully mimic a fully functional HR1 structure of S2, we asked whether these chimeric proteins could also reproduce immunogenic epitopes in S2 with relevance during SARS-CoV-2 infection. Thus, we tested the IgG and IgA reactivity against the CoVS-HR1 proteins in sera from convalescent patients collected three months after the onset of COVID-19. At that time, most patients' sera showed a sustained SARS-CoV-2-specific IgG response against both RBD (Fig. 6A) and nucleocapside protein and also displayed significant neutralizing activity [63]. Interestingly, we also detected significant IgG responses against the three protein variants. These responses were not detectable in the sera from uninfected donors, indicating a development of SARS-CoV-2-specific immune responses against HR1. Although the mean Ab response against L3C was slightly lower than against RBD, some patients displayed high levels of anti-L3C Abs, similar or higher than the anti-RBD Abs levels. Moreover, the mean IgG binding to the three protein variants clearly correlated positively with their relative conformational stability and inhibitory activity, with the most stable protein L3C showing the highest IgG binding, which strongly suggests that these epitopes are of conformational nature. This may explain why no immunogenic HR1 epitopes had been detected so far by peptide-based epitope scans.

Interestingly, the IgA reactivity in the sera against the L3C variant was even higher than against RBD (Fig. 6B). These results clearly indicate that the CoVS-HR1 mimetic proteins are antigenic and imitate functionally relevant HR1 epitopes in S2 that elicit strong Ab responses during the course of the infection. Furthermore, the respective antibody response directed against L3C and RBD was extremely different between IgG and IgA (Fig. 6C) further suggesting an intrinsically different B cell maturation process against these two antigens.

The high IgA titers against HR1 are intriguing. Interestingly, although IgG are about five times more abundant in serum than IgA,

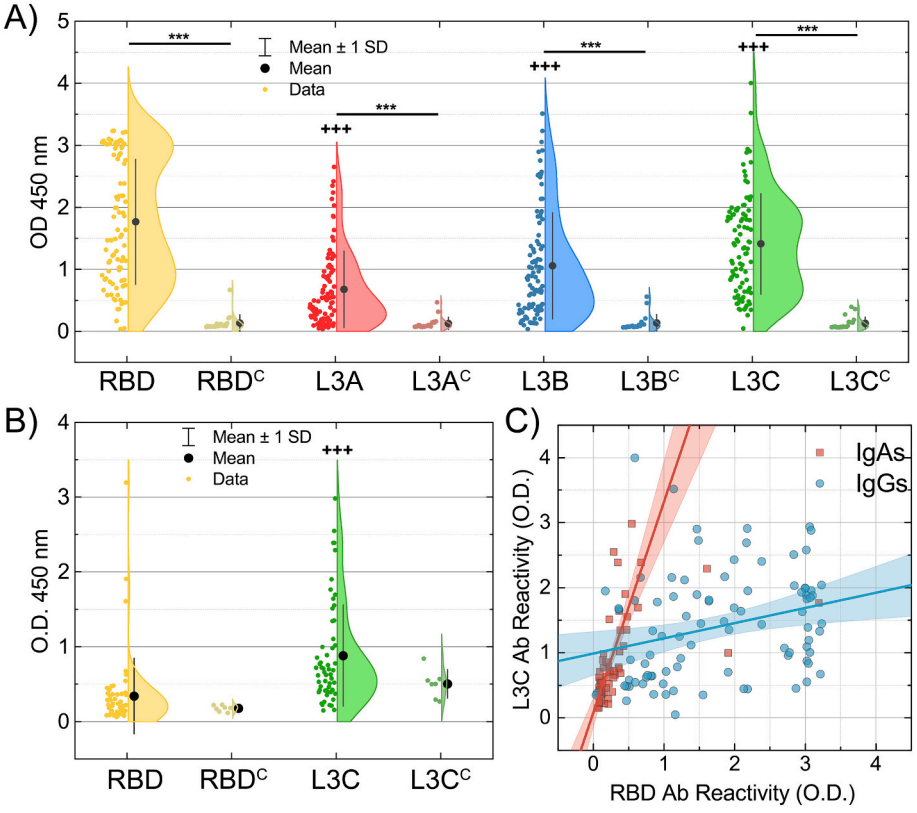

Fig. 6. Antigenicity of the CoVS-HR1 proteins against COVID-19 convalescent patient's sera. A) Reactivity levels of IgG against CoVS-HR1 proteins in infected patient sera 3 months after infection compared to reactivity against RBD. ELISA plates were coated with CoVS-HR1 proteins or His-tagged RDB and tested with 1/1000 diluted sera of patients for 30 min. Control sera from healthy patients were also tested (indicated with 'C' superscript). Antibody binding was measured with goat anti-human IgG antibody conjugated to horseradish peroxidase. B) Recognition levels of IgAs present in infected patient sera 3 months after infection towards CoVS-HR1-L3C compared to recognition to RBD. C) IgG and IgA reactivity against L3C protein vs RBD in convalescent plasma of SARS-CoV-2 patients. Linear regression and Anova test were performed with the following values: IgAs vs RDB: Pearson's r = 0.75; $p < 0.0001$; n = 53. IgGs vs RBD: Pearson's r = 0.29; $p > 0.05$; n = 90.

several studies showed higher neutralizing activities for IgA purified from sera of infected individuals compared to their IgG counterparts [64,65]. Whether IgA against HR1 display neutralizing function will need further investigation.

4. Discussion

Peptides derived from S2 HR1 region had been previously dismissed as potential fusion inhibitors [66] due to their intrinsic instability and high propensity to aggregate, similarly to that observed for gp41 HR1 in HIV-1. However, the stabilization of the HR1 trimeric coiled-coil structure has resulted in potent anti-HIV fusion inhibitors targeting HR2 [20,22]. We demonstrated here that a similar strategy also works for SARS-CoV-2 and, likely, for other related coronaviruses. A trimeric HR1 trimer design based of HIV-1 gp41-derived sequences has also shown a moderate but significant pan-coronavirus activity, suggesting relatively low specificity requisites for significant inhibition [23]. Our mimetic proteins specifically based on the SARS-CoV-2 S2 HR1 sequence constitute a novel approach to design this type of HR1-based fusion inhibitors targeting the highly conserved HR2 region. This approach is further supported by recent reports of a trimer of S2 HR1 polypeptides stabilized by conjugation to a foldon sequence [25], and a S2 postfusion-based 5-helix construct [24], both showing potent and broad inhibitory activities. Our strategy consisted however in engineering a single-chain polypeptide that can fold autonomously to mimic a highly stable HR1 surface, without any chemical modification or addition of external trimerization motifs. This makes these proteins very easy to produce and handle, strongly facilitating their development as potential drugs or vaccines.

Recent results pointed to an Omicron spike evolving beyond immune evasion towards a more compact architecture with a well-regulated fusion machinery, altered dynamics and easy to release fusion peptide [67]. Noteworthy, the CoVS-HR1 proteins showed similar inhibitory potency for BA.1 Omicron compared to the ancestral B.1 virus. Since the Omicron variant does not have any mutation at the HR2, it is likely that this preserved region is similarly exposed for both variants. On the other hand, BA.1 Omicron has three mutations at HR1, namely Q954H, N969K and L981F. Inspection of the equivalent amino acids in the L3B-V39E complex structure suggests that these amino acid substitutions, due to their conservative nature, should not have a strong impact on the HR1-HR2 interaction (Fig. S8), as also shown elsewhere [68]. Targeting these highly conserved fusion domains is therefore of strong therapeutic interest.

HR1 becomes transiently exposed after spike activation, since HR2 peptides are potent fusion inhibitors [66]. Nonetheless, it was previously unknown whether or not this exposure was sufficient to elicit a robust Ab response during infection. In fact, no significant Ab responses against HR1 had been reported so far. The strong Ab binding activity against the L3C CoVS-HR1 protein in the sera of convalescent patients indicates that HR1 epitopes are in fact immunogenic during the course of the disease, suggesting a frequent and stable epitope exposure. Also, the highest Ab response measured for L3C compared to the other two variants may be attributed to an improved Ab affinity for more stable HR1 epitopes displayed by L3C. This result, together with the fact that L3C contains the highest number of amino acid substitutions of the three variants, strongly suggests that the detected Ab responses are directed against HR1 conformational epitopes. This might be the reason why no neutralizing antibodies targeting HR1 have been reported because most studies use epitope mapping using linear peptides. Whether these HR1-targetting antibodies are neutralizing or not remains to be confirmed in future studies.

Elicitation of cryptic or transient conformational epitopes is a challenge for vaccine design. Protein structural scaffolds have been previously used to transplant complex epitopes that improve immunogenic responses [69–71]. A desirable property of these designs is a high structural stability that strongly correlates with antibody binding and with strong antigenicity. Here we show that our single-chain chimeric proteins can accurately mimic immunologically relevant and highly stable HR1 epitopes. The structural stability of these epitopes are clearly correlated with their inhibitory activity of cell infection by interacting with HR2, as well as with their antigenicity against antibodies developed during COVID-19 disease. These results make the CoVS-HR1 proteins potential candidates as novel potent therapeutics or new vaccine compositions against COVID-19.

CRediT authorship contribution statement

Mario Cano-Muñoz: Methodology, Investigation, Data curation, Formal analysis, Visualization. **Daniel Polo-Megías:** Methodology, Investigation, Data curation. **Ana Cámara-Artigas:** Investigation, Validation, Data curation, Formal analysis, Writing – review & editing. **José A. Gavira:** Investigation, Validation, Data curation. **María J. López-Rodríguez:** Investigation. **Géraldine Laumond:** Investigation. **Sylvie Schmidt:** Investigation. **Julien Demiselle:** Resources. **Seiamak Bahram:** Supervision, Funding acquisition. **Christiane Moog:** Conceptualization, Methodology, Data curation, Validation, Supervision, Funding acquisition, Project administration, Writing – review & editing. **Francisco Conejero-Lara:** Conceptualization, Methodology, Validation, Data curation, Formal analysis, Supervision, Funding acquisition, Project administration, Writing – original draft.

Declaration of competing interest

The University of Granada, the University of Strasbourg and the Institut National de la Santé et de la Recherche Médicale (INSERM) have filed a patent application (P202230188) on the chimeric proteins described in this article. Inventors: F.C-L., M.C-M. and C.M.

Data availability

The crystallographic structure of the CoVS-HR1-L3B protein in complex with the V39E peptide has been deposited at the Protein Data Bank with accession code 7ZR2. The data that support all the findings of this study are available from the corresponding authors on reasonable request; see author contributions for specific data sets.

Acknowledgments

This work was supported by grants CV20.26565 from the Consejería de Economía y Conocimiento, Junta de Andalucía (Spain), PID2019.107515RB.C21 from the Spanish State Research Agency (SRA/10.13039/501100011033), and co-funded by ERDF/ESF, “A way to make Europe”/“Investing in your future”. The work performed in C.M.’s laboratory was supported by grants from ANRS (Agence Nationale de Recherches sur le SIDA et les hépatites virales), the Investissements d’Avenir program managed by the ANR under reference ANR-10-LABX-77 and EHVA (No. 681032, Horizon 2020). Work in S.B.’s laboratory was supported by grants from the Agence Nationale de la Recherche (ANR) (ANR-11-LABX-0070_TRANSPLANTEX), the INSERM (UMR_S 1109), the Institut Universitaire de France (IUF), all the University of Strasbourg (IDEX UNISTRA), the European Regional Development Fund (European Union) INTERREG V program (project no. 3.2 TRIDIAG) and MSD-Avenir grant AUTOGEN. We are grateful to the Spanish Radiation Synchrotron Source (ALBA), Barcelona, Spain and the European Synchrotron Radiation Facility (ESRF), Grenoble, France, for the provision of time and staff assistance at XALOC (ALBA) and ID30B and ID23-2 (ESRF) beamlines during diffraction data collection. We thank María Carmen Salinas-García for her assistance in carrying out the crystallization screenings. We also thank Pilar González-García for helping us with the statistical analysis.

Appendix A. Supplementary data

Supplementary data to this article can be found online at https://doi.org/10.1016/j.ijbiomac.2022.10.031.

References

[1] H. Fathizadeh, S. Afshar, M.R. Masoudi, P. Gholizadeh, M. Asgharzadeh, K. Ganbarov, S. Kose, M. Yousefi, H.S. Kafil, SARS-CoV-2 (Covid-19) vaccines structure, mechanisms and effectiveness: a review, Int. J. Biol. Macromol. 188 (2021) 740–750, https://doi.org/10.1016/j.ijbiomac.2021.08.076.

[2] R.K. Gupta, Will SARS-CoV-2 variants of concern affect the promise of vaccines? Nat. Rev. Immunol. 21 (2021) 340–341, https://doi.org/10.1038/s41577-021-00556-5.

[3] S.S.A. Karim, Q.A. Karim, Omicron SARS-CoV-2 variant: a new chapter in the COVID-19 pandemic, Lancet 398 (2021) 2126–2128, https://doi.org/10.1016/s0140-6736(21)02758-6.

[4] D. Wrapp, N.S. Wang, K.S. Corbett, J.A. Goldsmith, C.L. Hsieh, O. Abiona, B. S. Graham, J.S. McLellan, Cryo-EM structure of the 2019-nCoV spike in the prefusion conformation, Science 367 (2020) 1260–1263, https://doi.org/10.1126/science.abb2507.

[5] Y.F. Cai, J. Zhang, T.S. Xiao, H.Q. Peng, S.M. Sterling, R.M. Walsh, S. Rawson, S. Rits-Volloch, B. Chen, Distinct conformational states of SARS-CoV-2 spike protein, Science 369 (2020) 1586–1592, https://doi.org/10.1126/science.abd4251.

[6] M. Hoffmann, H. Kleine-Weber, S. Schroeder, N. Krueger, T. Herrler, S. Erichsen, T. S. Schiergens, G. Herrler, N.-H. Wu, A. Nitsche, M.A. Mueller, C. Drosten, S. Poehlmann, SARS-CoV-2 cell entry depends on ACE2 and TMPRSS2 and is blocked by a clinically proven protease inhibitor, Cell 181 (2020) 271–280, https://doi.org/10.1016/j.cell.2020.02.052.

[7] M.A. Tortorici, D. Veesler, Structural insights into coronavirus entry, in: F.A. Rey (Ed.), Complementary Strategies to Understand Virus Structure and Function, 2019, pp. 93–116.

[8] S. Xia, M. Liu, C. Wang, W. Xu, Q. Lan, S. Feng, F. Qi, L. Bao, L. Du, S. Liu, C. Qin, F. Sun, Z. Shi, Y. Zhu, S. Jiang, L. Lu, Inhibition of SARS-CoV-2 (previously 2019-nCoV) infection by a highly potent pan-coronavirus fusion inhibitor targeting its spike protein that harbors a high capacity to mediate membrane fusion, Cell Res. 30 (2020) 343–355, https://doi.org/10.1038/s41422-020-0305-x.

[9] S. Xia, L. Yan, W. Xu, A.S. Agrawal, A. Algaissi, C.-T.K. Tseng, Q. Wang, L. Du, W. Tan, I.A. Wilson, S. Jiang, B. Yang, L. Lu, A pan-coronavirus fusion inhibitor targeting the HR1 domain of human coronavirus spike, Sci. Adv. 5 (2019), https://doi.org/10.1126/sciadv.aav4580.

[10] S. Laha, J. Chakraborty, S. Das, S.K. Manna, S. Biswas, R. Chatterjee, Characterizations of SARS-CoV-2 mutational profile, spike protein stability and viral transmission, Infect. Genet. Evol. 85 (2020), 104445, https://doi.org/10.1016/j.meegid.2020.104445.

[11] S.W. Liu, G.F. Xiao, Y.B. Chen, Y.X. He, J.K. Niu, C.R. Escalante, H.B. Xiong, J. Farmar, A.K. Debnath, P. Tien, S.B. Jiang, Interaction between heptad repeat 1 and 2 regions in spike protein of SARS-associated coronavirus: implications for virus fusogenic mechanism and identification of fusion inhibitors, Lancet 363 (2004) 938–947, https://doi.org/10.1016/s0140-6736(04)15788-7.

[12] P.V. Raghuvamsi, N.K. Tulsian, F. Samsudin, X.L. Qian, K. Purushotorman, G. Yue, M.M. Kozma, W.Y. Hwa, J. Lescar, P.J. Bond, P.A. MacAry, G.S. Anand, SARS-CoV-2 S protein:ACE2 interaction reveals novel allosteric targets, elife 10 (2021), e63646, https://doi.org/10.7554/eLife.63646.

[13] B. Turonova, M. Sikora, C. Schurmann, W.J.H. Hagen, S. Welsch, F.E.C. Blanc, S. von Bulow, M. Gecht, K. Bagola, C. Horner, G. van Zandbergen, J. Landry, N.T. D. de Azevedo, S. Mosalaganti, A. Schwarz, R. Covino, M.D. Muhlebach, G. Hummer, J.K. Locker, M. Beck, In situ structural analysis of SARS-CoV-2 spike reveals flexibility mediated by three hinges, Science 370 (2020) 203–208, https://doi.org/10.1126/science.abd5223.

[14] L. Casalino, Z. Gaieb, J.A. Goldsmith, C.K. Hjorth, A.C. Dommer, A.M. Harbison, C. A. Fogarty, E.P. Barros, B.C. Taylor, J.S. McLellan, E. Fadda, R.E. Amaro, Beyond shielding: the roles of glycans in the SARS-CoV-2 spike protein, ACS Central Sci. 6 (2020) 1722–1734, https://doi.org/10.1021/acscentsci.0c01056.

[15] Y. Watanabe, Z.T. Berndsen, J. Raghwani, G.E. Seabright, J.D. Allen, O.G. Pybus, J. S. McLellan, I.A. Wilson, T.A. Bowden, A.B. Ward, M. Crispin, Vulnerabilities in coronavirus glycan shields despite extensive glycosylation, Nat. Commun. 11 (2020) 2688, https://doi.org/10.1038/s41467-020-16567-0.

[16] B.J. Bosch, B.E.E. Martina, R. van der Zee, J. Lepault, B.J. Haijema, C. Versluis, A.J. R. Heck, R. de Groot, A. Osterhaus, P.J.M. Rottier, Severe acute respiratory syndrome coroavirus (SARS-CoV) infection inhibition using spike protein heptad repeat-derived peptides, Proc. Natl. Acad. Sci. U. S. A. 101 (2004) 8455–8460, https://doi.org/10.1073/pnas.0400576101.

[17] D. Schuetz, Y.B. Ruiz-Blanco, J. Muench, F. Kirchhoff, E. Sanchez-Garcia, J. A. Mueller, Peptide and peptide-based inhibitors of SARS-CoV-2 entry, Adv. Drug Deliv. Rev. 167 (2020) 47–65.

[18] J.M. Kilby, S. Hopkins, T.M. Venetta, B. DiMassimo, G.A. Cloud, J.Y. Lee, L. Alldredge, E. Hunter, D. Lambert, D. Bolognesi, T. Matthews, M.R. Johnson, M. A. Nowak, G.M. Shaw, M.S. Saag, Potent suppression of HIV-1 replication in humans by T-20, a peptide inhibitor of gp41-mediated virus entry, Nat. Med. 4 (1998) 1302–1307, https://doi.org/10.1038/3293.

[19] Y. He, Y. Xiao, H. Song, Q. Liang, D. Ju, X. Chen, H. Lu, W. Jing, S. Jiang, L. Zhang, Design and evaluation of sifuvirtide, a novel HIV-1 fusion inhibitor, J. Biol. Chem. 283 (2008) 11126–11134, https://doi.org/10.1074/jbc.M800200200.

[20] D.M. Eckert, P.S. Kim, Design of potent inhibitors of HIV-1 entry from the gp41 N-peptide region, Proc. Natl. Acad. Sci. U. S. A. 98 (2001) 11187–11192, https://doi.org/10.1073/pnas.201392898.

[21] M.J. Root, M.S. Kay, P.S. Kim, Protein design of an HIV-1 entry inhibitor, Science 291 (2001) 884–888, https://doi.org/10.1126/science.1057453.

[22] S. Crespillo, A. Camara-Artigas, S. Casares, B. Morel, E.S. Cobos, P.L. Mateo, N. Mouz, C.E. Martin, M.G. Roger, R. El Habib, B. Su, C. Moog, F. Conejero-Lara, Single-chain protein mimetics of the N-terminal heptad-repeat region of gp41 with potential as anti-HIV-1 drugs, Proc. Natl. Acad. Sci. U. S. A. 111 (2014) 18207–18212, https://doi.org/10.1073/pnas.1413592112.

[23] C. Wang, S. Xia, X. Wang, Y. Li, H. Wang, R. Xiang, Q. Jiang, Q. Lan, R. Liang, Q. Li, S. Huo, L. Lu, Q. Wang, F. Yu, K. Liu, S. Jiang, Supercoiling structure-based Design of a Trimeric Coiled-Coil Peptide with high potency against HIV-1 and human beta-coronavirus infection, J. Med. Chem. 65 (2021) 2809–2819, https://doi.org/10.1021/acs.jmedchem.1c00258.

[24] L. Xing, X. Xu, W. Xu, Z. Liu, X. Shen, J. Zhou, L. Xu, J. Pu, C. Yang, Y. Huang, L. Lu, S. Jiang, S. Liu, A five-helix-based SARS-CoV-2 fusion inhibitor targeting heptad repeat 2 domain against SARS-CoV-2 and its variants of concern, Viruses-Basel 14 (2022) 597, https://doi.org/10.3390/v14030597.

[25] W. Bi, G. Chen, B. Dang, Novel engineered SARS-CoV-2 HR1 trimer exhibits improved potency and broad-Spectrum activity against SARS-CoV-2 and its variants, J. Virol. (2022), https://doi.org/10.1128/jvi.00681-22.

[26] E. Bianchi, J.G. Joyce, M.D. Miller, A.C. Finnefrock, X. Liang, M. Finotto, P. Ingallinella, P. McKenna, M. Citron, E. Ottinger, R.W. Hepler, R. Hrin, D. Nahas, C. Wu, D. Montefiori, J.W. Shiver, A. Pessi, P.S. Kim, Vaccination with peptide mimetics of the gp41 prehairpin fusion intermediate yields neutralizing antisera against HIV-1 isolates, Proc. Natl. Acad. Sci. U. S. A. 107 (2010) 10655–10660, https://doi.org/10.1073/pnas.1004261107.

[27] D. Corti, J.P.M. Langedijk, A. Hinz, M.S. Seaman, F. Vanzetta, B.M. Fernandez-Rodriguez, C. Silacci, D. Pinna, D. Jarrossay, S. Balla-Jhagjhoorsingh, B. Willems, M.J. Zekveld, H. Dreja, E. O'Sullivan, C. Pade, C. Orkin, S.A. Jeffs, D.C. Montefiori, D. Davis, W. Weissenhorn, A. McKnight, J.L. Heeney, F. Sallusto, Q.J. Sattentau, R. A. Weiss, A. Lanzavecchia, Analysis of memory B cell responses and isolation of novel monoclonal antibodies with neutralizing breadth from HIV-1-infected individuals, PLoS One 5 (2010), e8805, https://doi.org/10.1371/journal.pone.0008805.

[28] C. Sabin, D. Corti, V. Buzon, M.S. Seaman, D.L. Huisik, A. Hinz, F. Vanzetta, G. Agatic, C. Silacci, L. Mainetti, G. Scarlatti, F. Sallusto, R. Weiss, A. Lanzavecchia, W. Weissenhorn, Crystal structure and size-dependent neutralization properties of HK20, a human monoclonal antibody binding to the highly conserved heptad repeat 1 of gp41, PLoS Pathog. 6 (2010), e1001195, https://doi.org/10.1371/journal.ppat.1001195.

[29] H.A. Elshabrawy, M.M. Coughlin, S.C. Baker, B.S. Prabhakar, Human monoclonal antibodies against highly conserved HR1 and HR2 domains of the SARS-CoV spike protein are more broadly neutralizing, PLoS One 7 (2012), e50366, https://doi.org/10.1371/journal.pone.0050366.

[30] H.W. Jiang, Y. Li, H.N. Zhang, W. Wang, X. Yang, H. Qi, H. Li, D. Men, J. Zhou, S. C. Tao, SARS-CoV-2 proteome microarray for global profiling of COVID-19 specific IgG and IgM responses, Nat. Commun. 11 (2020) 3581, https://doi.org/10.1038/s41467-020-17488-8.

[31] S. Ghotloo, F. Maghsood, F. Golsaz-Shirazi, M.M. Amiri, C. Moog, F. Shokri, Epitope mapping of neutralising anti-SARS-CoV-2 monoclonal antibodies: implications for immunotherapy and vaccine design, Rev. Med. Virol. (2022), https://doi.org/10.1002/rmv.2347 e2347-e2347.

[32] M. Sakharkar, C.G. Rappazzo, W.F. Wieland-Alter, C.L. Hsieh, D. Wrapp, E. S. Esterman, C.I. Kaku, A.Z. Wec, J.C. Geoghegan, J.S. McLellan, R.I. Connor, P. F. Wright, L.M. Walker, Prolonged evolution of the human B cell response to SARS-CoV-2 infection, Sci. Immunol. 6 (2021), https://doi.org/10.1126/sciimmunol.abg6916.

[33] S. Lusvarghi, S.D. Pollett, S.N. Neerukonda, W. Wang, R. Wang, R. Vassell, N. J. Epsi, A.C. Fries, B.K. Agan, D.A. Lindholm, C.J. Colombo, R. Mody, E.C. Ewers, T. Lalani, A. Ganesan, E. Goguet, M. Hollis-Perry, S.A.A. Coggins, M.P. Simons, L. C. Katzelnick, G. Wang, D.R. Tribble, L. Bentley, A.E. Eakin, C.C. Broder, K. J. Erlandson, E.D. Laing, T.H. Burgess, E. Mitre, C.D. Weiss, SARS-CoV-2 BA.1 variant is neutralized by vaccine booster-elicited serum, but evades most convalescent serum and therapeutic antibodies, Sci. Transl. Med. (2022), https://doi.org/10.1126/scitranslmed.abn8543 eabn8543-eabn8543.

[34] P. Shah, G.A. Canziani, E.P. Carter, I. Chaiken, The case for S2: the potential benefits of the S2 subunit of the SARS-CoV-2 spike protein as an immunogen in fighting the COVID-19 pandemic, Front. Immunol. 12 (2021), 637651, https://doi.org/10.3389/fimmu.2021.637651.

[35] K.W. Ng, N. Faulkner, G.H. Cornish, A. Rosa, R. Harvey, S. Hussain, R. Ufferts, C. Earl, A.G. Wrobel, D.J. Benton, C. Roustan, W. Bolland, R. Thompson, A. Agua-Doce, P. Hobson, J. Heaney, H. Rickman, S. Paraskevopoulou, C.F. Houlihan, K. Thomson, E. Sanchez, G.Y. Shin, M.J. Spyer, D. Joshi, N. O'Reilly, P.A. Walker, S. Kjaer, A. Riddell, C. Moore, B.R. Jebson, M. Wilkinson, L.R. Marshall, E. C. Rosser, A. Radziszewska, H. Peckham, C. Ciurtin, L.R. Wedderburn, R. Beale, C. Swanton, S. Gandhi, B. Stockinger, J. McCauley, S.J. Gambill, L.E. McCoy, P. Cherepanov, E. Nastouli, G. Kassiotis, Preexisting and de novo humoral immunity to SARS-CoV-2 in humans, Science 370 (2020) 1339–1343, https://doi.org/10.1126/science.abe1107.

[36] N.-C. Phuong, A.K. Embong, P. Kanagaiah, F.A. Chaves, H. Yang, A.R. Branche, D. J. Topham, M.Y. Sangster, S Protein-reactive IgG and memory B cell production

after human SARS-CoV-2 infection includes broad reactivity to the S2 subunit, Mbio 11 (2020), https://doi.org/10.1128/mBio.01991-20 e01991-01920.
[37] L. Farrera-Soler, J.-P. Daguer, S. Barluenga, N. Winssinger, Experimental identification of immuno- dominant B-cell epitopes from SARS-CoV-2, Chimia 75 (2021) 276–284, https://doi.org/10.2533/chimia.2021.276.
[38] Y. Li, D.-Y. Lai, H.-N. Zhang, H.-W. Jiang, X. Tian, M.-L. Ma, H. Qi, Q.-F. Meng, S.-J. Guo, Y. Wu, W. Wang, X. Yang, D.-W. Shi, J.-B. Dai, T. Ying, J. Zhou, S.-C. Tao, Linear epitopes of SARS-CoV-2 spike protein elicit neutralizing antibodies in COVID-19 patients, Cell. Mol. Immunol. 17 (2020) 1095–1097, https://doi.org/10.1038/s41423-020-00523-5.
[39] P. Zhou, M. Yuan, G. Song, N. Beutler, N. Shaabani, D. Huang, W.-T. He, X. Zhu, S. Callaghan, P. Yong, F. Anzanello, L. Peng, J. Ricketts, M. Parren, E. Garcia, S. A. Rawlings, D.M. Smith, D. Nemazee, J.R. Teijaro, T.F. Rogers, I.A. Wilson, D. R. Burton, R. Andrabi, A ProtectiveBroadly Cross-reactive Human Antibody Defines a Conserved Site of Vulnerabilityon Beta-coronavirus Spikes, bioRxiv : the preprint server for biology, 2021, https://doi.org/10.1101/2021.03.30.437769.
[40] M. Cano-Munoz, S. Cesaro, B. Morel, J. Lucas, C. Moog, F. Conejero-Lara, Extremely thermostabilizing Core mutations in coiled-coil mimetic proteins of HIV-1 gp41 produce diverse effects on target binding but do not affect their inhibitory activity, Biomolecules 11 (2021) 566, https://doi.org/10.3390/biom11040566.
[41] M. Cano-Munoz, S. Jurado, B. Morel, F. Conejero-Lara, Conformational flexibility of the conserved hydrophobic pocket of HIV-1 gp41. Implications for the discovery of small-molecule fusion inhibitors, Int. J. Biol. Macromol. 192 (2021) 90–99, https://doi.org/10.1016/j.ijbiomac.2021.09.198.
[42] S. Jurado, M. Cano-Munoz, B. Morel, S. Standoli, E. Santarossa, C. Moog, S. Schmidt, G. Laumond, A. Camara-Artigas, F. Conejero-Lara, Structural and thermodynamic analysis of HIV-1 fusion inhibition using small gp41 mimetic proteins, J. Mol. Biol. 431 (2019) 3091–3106, https://doi.org/10.1016/j.jmb.2019.06.022.
[43] S. Jurado, M. Cano-Munoz, D. Polo-Megias, F. Conejero-Lara, B. Morel, Thermodynamic dissection of the interface between HIV-1 gp41 heptad repeats reveals cooperative interactions and allosteric effects, Arch. Biochem. Biophys. 688 (2020), 108401, https://doi.org/10.1016/j.abb.2020.108401.
[44] S. Jurado, C. Moog, M. Cano-Munoz, S. Schmidt, G. Laumond, V. Ruocco, S. Standoli, D. Polo-Megias, F. Conejero-Lara, B. Morel, Probing vulnerability of the gp41 C-terminal heptad repeat as target for miniprotein HIV inhibitors, J. Mol. Biol. 432 (2020) 5577–5592, https://doi.org/10.1016/j.jmb.2020.08.010.
[45] M. Cano-Munoz, J. Lucas, L.-Y. Lin, S. Cesaro, C. Moog, F. Conejero-Lara, Conformational stabilization of Gp41-mimetic miniproteins opens up new ways of inhibiting HIV-1 fusion, Int. J. Mol. Sci. 23 (2022) 2794, https://doi.org/10.3390/ijms23052794.
[46] N. Guex, M.C. Peitsch, SWISS-MODEL and the swiss-PdbViewer: an environment for comparative protein modeling, Electrophoresis 18 (1997) 2714–2723, https://doi.org/10.1002/elps.1150181505.
[47] E. Krieger, G. Vriend, YASARA view - molecular graphics for all devices - from smartphones to workstations, Bioinformatics 30 (2014) 2981–2982, https://doi.org/10.1093/bioinformatics/btu426.
[48] Y. Liu, B. Kuhlman, RosettaDesign server for protein design, Nucleic Acids Res. 34 (2006) W235–W238, https://doi.org/10.1093/nar/gkl163.
[49] E. Gasteiger, A. Gattiker, C. Hoogland, I. Ivanyi, R.D. Appel, A. Bairoch, ExPASy: the proteomics server for in-depth protein knowledge and analysis, Nucleic Acids Res. 31 (2003) 3784–3788, https://doi.org/10.1093/nar/gkg563.
[50] A. Ortega, D. Amoros, J. Garcia de la Torre, Prediction of hydrodynamic and other solution properties of rigid proteins from atomic- and residue-level models, Biophys. J. 101 (2011) 892–898, https://doi.org/10.1016/j.bpj.2011.06.046.
[51] J. Juanhuix, F. Gil-Ortiz, G. Cuni, C. Colldelram, J. Nicolas, J. Lidon, E. Boter, C. Ruget, S. Ferrer, J. Benach, Developments in optics and performance at BL13-XALOC, the macromolecular crystallography beamline at the ALBA synchrotron, J. Synchrot. Radiat. 21 (2014) 679–689, https://doi.org/10.1107/S160057751400825X.
[52] C. Vonrhein, C. Flensburg, P. Keller, A. Sharff, O. Smart, W. Paciorek, T. Womack, G. Bricogne, Data processing and analysis with the autoPROC toolbox, Acta Crystallogr. Sect. D-Biol. Crystallogr. 67 (2011) 293–302, https://doi.org/10.1107/S0907444911007773.
[53] P.R. Evans, An introduction to data reduction: space-group determination, scaling and intensity statistics, Acta Crystallogr. Sect. D-Biol. Crystallogr. 67 (2011) 282–292, https://doi.org/10.1107/S090744491003982X.
[54] N. <collab>Collaborative Computational Project, The CCP4 suite: programs for protein crystallography, Acta Crystallogr. Sect. D-Biol. Crystallogr. 50 (1994) 760–763, https://doi.org/10.1107/S0907444994003112.
[55] P.D. Adams, P.V. Afonine, G. Bunkoczi, V.B. Chen, I.W. Davis, N. Echols, J. J. Headd, L.W. Hung, G.J. Kapral, R.W. Grosse-Kunstleve, A.J. McCoy, N. W. Moriarty, R. Oeffner, R.J. Read, D.C. Richardson, J.S. Richardson, T. C. Terwilliger, P.H. Zwart, PHENIX: a comprehensive python-based system for macromolecular structure solution, Acta Crystallogr. Sect. D-Biol. Crystallogr. 66 (2010) 213–221, https://doi.org/10.1107/S0907444909052925.
[56] G. Bunkoczi, N. Echols, A.J. McCoy, R.D. Oeffner, P.D. Adams, R.J. Read, Phaser. MRage, Automated molecular replacement, Acta Crystallogr. Sect. D-Biol. Crystallogr. 69 (2013) 2276–2286, https://doi.org/10.1107/S0907444913022750.
[57] P. Emsley, K. Cowtan, Coot: model-building tools for molecular graphics, Acta Crystallogr. Sect. D-Biol. Crystallogr. 60 (2004) 2126–2132, https://doi.org/10.1107/S0907444904019158.
[58] P. Emsley, B. Lohkamp, W.G. Scott, K. Cowtan, Features and development of coot, Acta Crystallogr. Sect. D-Biol. Crystallogr. 66 (2010) 486–501, https://doi.org/10.1107/S0907444910007493.
[59] P.V. Afonine, R.W. Grosse-Kunstleve, N. Echols, J.J. Headd, N.W. Moriarty, M. Mustyakimov, T.C. Terwilliger, A. Urzhumtsev, P.H. Zwart, P.D. Adams, Towards automated crystallographic structure refinement with phenix.Refine, Acta Crystallogr. Sect. D-Biol. Crystallogr. 68 (2012) 352–367, https://doi.org/10.1107/S0907444912001308.
[60] V.B. Chen, W.B. Arendall 3rd, J.J. Headd, D.A. Keedy, R.M. Immormino, G. J. Kapral, L.W. Murray, J.S. Richardson, D.C. Richardson, MolProbity: all-atom structure validation for macromolecular crystallography, Acta Crystallogr. Sect. D-Biol. Crystallogr. 66 (2010) 12–21, https://doi.org/10.1107/S0907444909042073.
[61] I. de Vries, T. Kwakman, X.J. Lu, M.L. Hekkelman, M. Deshpande, S. Velankar, A. Perrakis, R.P. Joosten, New restraints and validation approaches for nucleic acid structures in PDB-REDO, Acta Crystallogr. Sect. D-Biol. Crystallogr. 77 (2021) 1127–1141, https://doi.org/10.1107/s2059798321007610.
[62] P. Luo, R.L. Baldwin, Mechanism of helix induction by trifluoroethanol: a framework for extrapolating the helix-forming properties of peptides from trifluoroethanol/water mixtures back to water, Biochemistry 36 (1997) 8413–8421, https://doi.org/10.1021/bi9707133.
[63] R. Carapito, R. Li, J. Helms, C. Carapito, S. Gujja, V. Rolli, R. Guimaraes, J. Malagon-Lopez, P. Spinnhirny, A. Lederle, R. Mohseninia, A. Hirschler, L. Muller, P. Bastard, A. Gervais, Q. Zhang, F. Danion, Y. Ruch, M. Schenck, O. Collange, T.-N. Chamaraux-Tran, A. Molitor, A. Pichot, A. Bernard, O. Tahar, S. Bibi-Triki, H. Wu, N. Paul, S. Mayeur, A. Larnicol, G. Laumond, J. Frappier, S. Schmidt, A. Hanauer, C. Macquin, T. Stemmelen, M. Simons, X. Mariette, O. Hermine, S. Fafi-Kremer, B. Goichot, B. Drenou, K. Kuteifan, J. Pottecher, P.-M. Mertes, S. Kailasan, M.J. Aman, E. Pin, P. Nilsson, A. Thomas, A. Viari, D. Sanlaville, F. Schneider, J. Sibilia, P.-L. Tharaux, J.-L. Casanova, Y. Hansmann, D. Lidar, M. Radosavljevic, J.R. Gulcher, F. Meziani, C. Moog, T.W. Chittenden, S. Bahram, Identification of driver genes for critical forms of COVID-19 in a deeply phenotyped young patient cohort, Sci. Transl. Med. (2021), eabj7521-eabj7521, https://doi.org/10.1126/scitranslmed.abj7521.
[64] D. Sterlin, A. Malaussena, G. Gorochov, IgA dominates the early neutralizing antibody response to SARS-CoV-2 virus, Med. Sci. 37 (2021) 968–970, https://doi.org/10.1051/medsci/20211154.
[65] C. Planchais, I. Fernandez, T. Bruel, G.D. de Melo, M. Prot, M. Beretta, P. Guardado-Calvo, J. Dufloo, L.M. Molinos-Albert, M. Backovic, J. Chiaravalli, E. Giraud, B. Vesin, L. Conquet, L. Grzelak, D. Planas, I. Staropoli, F. Guivel-Benhassine, T. Hieu, M. Boulle, M. Cervantes-Gonzalez, M.-N. Ungeheuer, P. Charneau, S. van der Werf, F. Agou, J.D. Dimitrov, E. Simon-Loriere, H. Bourhy, X. Montagutelli, F.A. Rey, O. Schwartz, H. Mouquet, C.C.S.G. <collab>French </collab>, C.S. <collab>Group </collab>, Potent human broadly SARS-CoV-2-neutralizing IgA and IgG antibodies effective against Omicron BA.1 and BA.2, J. Exp. Med. 219 (2022), https://doi.org/10.1084/jem.20220638.
[66] S. Xia, Y. Zhu, M. Liu, Q. Lan, W. Xu, Y. Wu, T. Ying, S. Liu, Z. Shi, S. Jiang, L. Lu, Fusion mechanism of 2019-nCoV and fusion inhibitors targeting HR1 domain in spike protein, Cell. Mol. Immunol. 17 (2020) 765–767, https://doi.org/10.1038/s41423-020-0374-2.
[67] S.M.C. Gobeil, R. Henderson, V. Stalls, K. Janowska, X. Huang, A. May, M. Speakman, E. Beaudoin, K. Manne, D. Li, R. Parks, M. Barr, M. Deyton, M. Martin, K. Mansouri, R.J. Edwards, G.D. Sempowski, K.O. Saunders, K. Wiehe, W. Williams, B. Korber, B.F. Haynes, P. Acharya, Structural Diversity of the SARS-CoV-2 Omicron Spike, bioRxiv : the preprint server for biology, 2022, https://doi.org/10.1101/2022.01.25.477784.
[68] K.L. Yang, C.C. Wang, K.I. White, R.A. Pfuetzner, L. Esquivies, A.T. Brunger, Structural conservation among variants of the SARS-CoV-2 spike postfusion bundle, Proc. Natl. Acad. Sci. U. S. A. 119 (2022), https://doi.org/10.1073/pnas.2119467119.
[69] G. Ofek, F.J. Guenaga, W.R. Schief, J. Skinner, D. Baker, R. Wyatt, P.D. Kwong, Elicitation of structure-specific antibodies by epitope scaffolds, Proc. Natl. Acad. Sci. U. S. A. 107 (2010) 17880–17887, https://doi.org/10.1073/pnas.1004728107.
[70] M.L. Azoitei, B.E. Correia, Y.-E.A. Ban, C. Carrico, O. Kalyuzhniy, L. Chen, A. Schroeter, P.-S. Huang, J.S. McLellan, P.D. Kwong, D. Baker, R.K. Strong, W. R. Schief, Computation-guided backbone grafting of a discontinuous motif onto a protein scaffold, Science 334 (2011) 373–376, https://doi.org/10.1126/science.1209368.
[71] F. Sesterhenn, C. Yang, J. Bonet, J.T. Cramer, X. Wen, Y. Wang, C.-I. Chiang, L. A. Abriata, I. Kucharska, G. Castoro, S.S. Vollers, M. Galloux, E. Dheilly, S. Rosset, P. Corthesy, S. Georgeon, M. Villard, C.-A. Richard, D. Descamps, T. Delgado, E. Oricchio, M.-A. Rameix-Welti, V. Mas, S. Ervin, J.-F. Eleouet, S. Riffault, J. T. Bates, J.-P. Julien, Y. Li, T. Jardetzky, T. Krey, B.E. Correia, De novo protein design enables the precise induction of RSV-neutralizing antibodies, Science 368 (2020), eaay5051, https://doi.org/10.1126/science.aay5051.
[72] A.S. Konagurthu, J.C. Whisstock, P.J. Stuckey, A.M. Lesk, MUSTANG: a multiple structural alignment algorithm, Proteins 64 (2006) 559–574, https://doi.org/10.1002/prot.20921.